Survey of classical density functionals for modelling hydrogen physisorption at 77 K

Survey of classical density functionals for modelling hydrogen physisorption at 77 K

M. B. Sweatman
Department of Chemical and Process Engineering, University of Strathclyde, Glasgow, G1 1XJ, United Kingdom
(Received 30 November 2007; published 28 February 2008)

This work surveys techniques based on classical density functionals for modeling the quantum dispersion of physisorbed hydrogen at 77 K. Two such techniques are examined in detail. The first is based on the "open ring approximation" (ORA) of Broukhno *et al.*, and it is compared with a technique based on the semiclassical approximation of Feynman and Hibbs (FH). For both techniques, a standard classical density functional is used to model hydrogen molecule–hydrogen molecule (i.e., excess) interactions. The three-dimensional (3D) quantum harmonic oscillator (QHO) system and a model of molecular hydrogen adsorption into a graphitic slit pore at 77 K are used as benchmarks. Density functional results are compared with path-integral Monte Carlo simulations and with exact solutions for the 3D QHO system. It is found that neither of the density functional treatments are entirely satisfactory. However, for hydrogen physisorption studies at 77 K the ORA based technique is generally superior to the FH based technique due to a fortunate cancellation of errors in the density functionals used. But, if more accurate excess functionals are used, the FH technique would be superior.

DOI: 10.1103/PhysRevE.77.026712 PACS number(s): 05.10.−a, 68.43.De, 05.20.Jj, 67.63.Cd

I. INTRODUCTION

The path-integral (PI) formulation of quantum mechanics [1] allows equilibrium quantum particles to be represented as unusual classical ring polymers. This mapping converges to the exact quantum mechanical result in the limit that n, the number of sites on a single ring-polymer ring, tends to infinity. This ring-polymer representation is very convenient and invites [2,3] the techniques of classical statistical mechanics to be used to solve some quantum problems.

Path integral simulations, both Monte Carlo (PI-MC) and molecular dynamics (PI-MD), are popular in this context and provide accurate information that are in principle exact (to within statistical error) for a given n. But these methods can be computationally demanding, especially for large n. So, theoretical alternatives to simulation are often useful. In the field of classical fluids density functional theory (DFT) is a powerful tool with a wide range of applications, including simple fluids, polymers, colloids, etc. For situations with significant symmetry, for example those involving spherical particles adsorbed into slit or cylindrical pores, etc., DFT calculations can be up to several orders of magnitude more efficient, sometimes without significant loss of accuracy, compared to simulation. Hard spheres in slit pores are a good example here; hard-sphere DFTs are often solved in a few seconds on a desktop PC, whereas corresponding MC simulations might take several minutes to obtain a satisfactory level of precision. Path-integral simulations are more demanding still. So DFT is an attractive technique, not only for gaining fundamental theoretical understanding, where absolute accuracy is not essential, but also for engineering applications (optimization studies, for example) where calculation efficiency must be weighed against accuracy.

Consequently, in recent years, several studies have attempted to apply the classical version of density functional theory to model quantum particles via the PI–classical ring-polymer mapping [3], resulting in several approximate path-integral density functional theories (PI-DFTs). The aim of these studies is to develop finite-temperature DFT techniques that, for situations where the symmetries mentioned above allow, are significantly more efficient than the corresponding Monte Carlo approach. They require the development of classical density functionals for these unusual ring polymers.

For example, Broukhno *et al.* [4] recently developed a PI-DFT based on what they call the "open ring approximation" (ORA), which equates any site in a ring polymer with the middle site in the corresponding chain polymer. The chain-polymer problem is then easily solved exactly using the propagator approach of Woodward [5], which is also described below. They claim that their approximation becomes exact in the same limit that the PI technique becomes exact, i.e., $n \to \infty$, and validate their method by comparison with exact results for some simple spherically symmetric systems, including the 3D quantum harmonic oscillator (QHO) and the ground state of the hydrogen atom. They claim that their excellent results validate the ORA. Their results are impressive, if taken at face value, and suggest that their PI-DFT could find wide application. However, in fact the ORA is flawed and produces the wrong limit as $n \to \infty$. In other words, the statistics of ring and chain polymers are not equivalent in this limit. This result has been known for a long time [6,7]. Their technique is described below (in its corrected form) and their results for the 3D QHO are confirmed. It is also shown how this ORA technique, and indeed any PI-DFT technique based on classical density functionals for ring polymers, can be extended to model adsorption in the grand canonical ensemble. Results for the hydrogen adsorption problem demonstrate that the ORA is not generally accurate.

The above PI-DFT technique is compared with one based on the well-known semiclassical Feynman-Hibbs approximation [1]. This method quickly generates approximate interaction potentials, which can then be combined with a classical DFT to study grand canonical adsorption including the effect of quantum dispersion. A similar approach has been used in several [8–10] recent studies of hydrogen physisorption on graphitic surfaces, although in each of these studies simulation (either Monte Carlo or molecular dynamics) rather than classical DFT was combined with the FH technique, and the

actual density profiles were not derived or shown. The work described below is the first example where the FH approximation is combined with a classical DFT for nonuniform fluids (which is used to model "excess" interactions, i.e., hydrogen molecule–hydrogen molecule interactions), and it is shown how density profiles that include dispersion can be obtained. It is found that the FH technique performs well for low density physisorption of molecular hydrogen on a graphitic surface, although the mean-field density functional used to model excess interactions introduces some error at higher densities.

The work of Broukhno *et al.* is not the first application of classical ring-polymer density functionals to this problem. Gu *et al.* [11] also developed a density functional theory for ring polymers, this time based on a particular version [12] of "statistical associating fluid theory" (SAFT) that deals with ring polymers. However, because SAFT is a perturbation theory their ring-polymer model does not correspond to the PI–ring-polymer mapping. Their model consists of hard-sphere sites joined together to form a ring. Interactions between hard-sphere sites are allowed both within a single ring polymer and between all sites on different ring polymers. In a PI ring polymer interactions within a ring polymer should be limited to harmonic bonds between adjacent sites, and only sites with the same index (or label) interact with each other on different ring polymers. These are very different ring polymer models. No attempt is made to describe their method or reproduce their results here, but comparison is made between the results of the techniques examined in this work and their published results. It is found that their work is seriously flawed. Not only does their PI–DFT not correspond to the PI—ring-polymer mapping, but their grand canonical PI-MC simulation results, which they used to validate their theory, are also found to be qualitatively incorrect.

Note that the first [13] density functional theory for nonuniform ring polymers was based on a weighted density approximation (WDA) for bonding. In that work it was suggested that this ring-polymer DFT could be adapted to model quantum dispersion. Although this turns out to be true [14], this approach also suffers a serious problem. The problem is that this particular DFT for ring polymers is approximate, and so it does not generate results that converge to a limit as $n \to \infty$. In a sense this is worse than the ORA of Broukhno *et al.*, which only converges to the wrong limit. By fine-tuning n in this technique it is possible to calibrate this WDA-based PI-DFT, but the calibration process is inconvenient and results produced by this method do not offer any significant advantage over the Feynman-Hibbs based method for hydrogen physisorption on a graphitic surface at 77 K. Consequently, it is not presented here.

Finally, path-integral Monte Carlo (PI-MC) simulation, both its canonical and grand-canonical versions, is used as a benchmark to test the density functionals for the hydrogen adsorption problem. This PI-MC algorithm is itself validated by comparison with exact results for the 3D-QHO system.

Two tests are employed in this work to compare the techniques described above. One test is a system consisting of single quantum particle in a 3D harmonic oscillator at finite temperature, for which exact results are easily obtained (see Appendix A). The second is a model of hydrogen adsorption in graphitic slit pores at 77 K. At this temperature the thermal de Broglie wavelength of molecular hydrogen is 0.14 nm, which is more than twice the lengthscale of the hydrogen-graphite interaction ($\sim$0.06 nm) but less than half the average interparticle separation at the highest hydrogen densities considered in this work ($\sim$0.34 nm). This means that quantum effects should be significant with respect to the hydrogen-graphite interaction but they should not be significant with respect to hydrogen-hydrogen interactions. In other words, molecular hydrogen at 77 K adsorbed onto graphitic surfaces will exhibit significant quantum dispersion but not significant quantum exchange, and so presents a suitable test case for the DFT techniques presented here. Moreover, studies of molecular hydrogen physisorption have received a great deal of attention, particularly over the last decade or so, in line with research into the "hydrogen economy" and especially hydrogen storage [15]. It is known that significant quantities of hydrogen, at either elevated pressure or reduced temperature (or both) [16], can be stored when physisorbed in microporous materials. But to discover an optimal adsorbent material together with optimal conditions of temperature and pressure is a challenge that still consumes a great deal of effort [17].

One of the difficulties in this respect is the quantum nature of hydrogen at low temperature. A range of techniques have been used to model these quantum effects, from PI-MC simulations [18,19] to more efficient approximate techniques based on the Feynman-Hibbs (FH) approach combined with Monte Carlo or molecular dynamics simulations. Stan and Cole [20] also used the FH approach to model hydrogen adsorption, but only considered the low density limit where excess interactions are absent, while Kowalczyk and MacElroy [21] combined the FH technique with a standard DFT describing excess interactions but only considered the bulk limit. Gu *et al.* [11] developed the first PI-DFT technique based on classical density functionals for nonuniform fluids, although as described earlier, their method is flawed. So the work described below is the first serious attempt to model the quantum dispersion of hydrogen adsorption at 77 K using only techniques based on classical density functionals.

The remainder of this paper is structured as follows. The theory section briefly describes each of the techniques above. The test systems are described in detail, and results for these test systems are presented and compared for each technique. The paper is concluded with a discussion.

II. THEORY

Path integral theory can be used to represent quantum particles at equilibrium as unusual classical ring polymers. The mapping is exact in the limit that n, the number of sites on each ring polymer, tends to infinity. These ring polymers are unusual because of their interactions; in the absence of exchange interactions intrapolymer interactions occur only between adjacent sites (which are labeled $1, \ldots, n$ with site 1 being adjacent to site n) and can be taken to be springlike in form, while interpolymer interactions occur only between sites with the same label and have $1/n$th the strength of the bare interparticle interaction, ϕ. Likewise, each site interacts

with an external field, V^{ext}, but only with $1/n$th the strength of the original potential. In the absence of exchange interactions these ring-polymers particles obey classical Boltzmann statistics, so for N identical "Boltzmannons" the partition function is

$$Q = \frac{1}{N!}\left(\frac{n\beta\lambda}{\pi}\right)^{3Nn/2} \int d\mathbf{R}_1 \ldots d\mathbf{R}_N \times \exp[-\beta(H^{intra} + H^{inter} + H^{\text{ext}})], \quad (1)$$

where the intrapolymer, interpolymer, and external potential contributions to the Hamiltonian are, respectively,

$$H^{\text{intra}} = \sum_{i=1}^{N} H^{\text{intra}}(\mathbf{R}_i) = n\lambda \sum_{i=1}^{N} \sum_{j=1}^{n} r_{ij\cdot ij+1}^2, \quad (2)$$

$$H^{\text{inter}} = \frac{1}{n} \sum_{i<j} \sum_{k=1}^{n} \phi(r_{ik\cdot jk}), \quad (3)$$

$$H^{\text{ext}} = \sum_{i=1}^{N} H^{\text{ext}}(\mathbf{R}_i) = \frac{1}{n} \sum_{i=1}^{N} \sum_{j=1}^{n} V^{\text{ext}}(\mathbf{r}_{ij}). \quad (4)$$

Here, $2n\lambda = mn/(\beta\hbar)^2$ is the "spring constant" of the intramolecular interactions, $\hbar$ is Planck's constant divided by 2π, $\beta = 1/k_BT$ (where T is the temperature), m is the particle's mass, $\mathbf{R}_i = \{\mathbf{r}_{i1}, \mathbf{r}_{i2}, \ldots, \mathbf{r}_{\text{in}}\}$ is the set of coordinates for the sites of the ith ring polymer, $r_{ik\cdot jl} = |\mathbf{r}_{ik} - \mathbf{r}_{jl}|$ is the separation between the kth site on the ith ring polymer and the lth site on the jth ring polymer, and $\mathbf{r}_{\text{in}+1} = \mathbf{r}_{i1}$ to create the rings. Essentially, the total interparticle and external potential interaction energies are averaged over the path of the ring polymer. This path is, for an isolated ring polymer, rather like a random 3D walk of steps with a range of lengths consistent with the intramolecular springlike bonds (it is not a perfectly random path because the final site is adjacent to the first). Note the thermal de Broglie wavelength $\Lambda = \sqrt{\pi/\beta\lambda}$.

Following Woodward [5], the exact Helmholtz free energy for the system of PI ring polymers is expressed in terms of the *ring polymer* density $\rho(\mathbf{R})$,

$$F = F^{id} + F^b + F^{\text{ext}} + F^{\text{ex}} = k_BT \int d\mathbf{R}\, \rho(\mathbf{R})\{\ln[(\pi/\beta\lambda)^{3/2}\rho(\mathbf{R})] - 1\} + \int \rho(\mathbf{R}) V^{\text{intra}}(\mathbf{R}) + \int \rho(\mathbf{R}) V^{\text{ext}}(\mathbf{R}) + F^{\text{ex}}, \quad (5)$$

where V^{intra} and V^{ext} are the intramolecular and external potentials for a single ring polymer [obtained by setting $N=1$ in Eqs. (2) and (4)]. Here, the first term is the ideal contribution for a gas consisting of molecules which are formed from n sites each, the second term accounts for the harmonic bonds between adjacent sites on each ring polymer and bonds the appropriate sites together to form a ring, the third term accounts for the interaction with the external potential, while the last "excess" term describes interactions between different ring polymers. Although an elegant formulation, the problem with this approach is the description of a ring polymer in terms of $\mathbf{R}$, which can have very many dimensions.

An alternative representation of this system can be obtained based on the interaction-site density functional formalism of Chandler *et al.* [22,23]. Here, the exact Helmholtz free energy density functional is written in terms of the total site density $\rho_s(\mathbf{r})$,

$$F = F^{id} + F^{\text{ext}} + F^b + F^{\text{ex}} = k_BT \int d\mathbf{r}\, \rho_s(\mathbf{r})\{\ln[(\pi/n\beta\lambda)^{3/2}\rho_s(\mathbf{r})] - 1\} + \frac{1}{n}\int \rho_s(\mathbf{r}) V^{\text{ext}}(\mathbf{r}) + F^b + F^{\text{ex}}. \quad (6)$$

Once again, the first term on the right is the ideal gas contribution, the next term accounts for the interaction with an external potential, the third term accounts for bonded interactions, and the last term describes all other interactions. The advantage of this description is that, because $\mathbf{r}$ has far fewer dimensions than $\mathbf{R}$, techniques based on it could potentially be as efficient as DFTs for simple fluids (which area also described in terms of $\mathbf{r}$). However, contrary to the Woodward approach, with this interaction-site approach an exact and compact expression is lacking for the bonding functional. This is a serious disadvantage because for the ring-polymer—PI mapping we prefer the ring-polymer density functional to converge to a fixed limit, close to the exact limit, as $n \to \infty$. Yet, because any bonding functional is necessarily approximate with this approach, this is not guaranteed. So PI-DFT techniques based on this approach could suffer serious problems, like the WDA-based method mentioned earlier.

A. Open ring approximation

Broukhno *et al.* explain that an exact solution of the ideal (i.e., ignoring the excess functional F^{ex}) PI ring-polymer problem corresponding to Eq. (5) can be achieved but only at considerable computational expense. The difficulty, compared to chain polymers, arises because of the need to ensure that the polymer forms a ring, which requires one to keep track of where the "beginning" and "end" points of a ring are. In the general case this presents severe computational difficulties, although for systems with reduced symmetry, such as fluids with spherical particles adsorbed on planar surfaces, calculations should be much less demanding. Because of this, Broukno *et al.* are able to solve the exact PI ring-polymer problem for a single particle in a 1D-QHO quite straightforwardly.

To model PI ring polymers more generally Broukhno *et al.* use the Woodward propagator approach described above and what they call the "open ring approximation" (ORA). The ORA equates the site density for any site in a ring polymer with an odd number of sites with the site density of the middle site in the corresponding chain polymer. Using the ORA and Woodward's propagator technique, the density of this middle site is given exactly (see Appendix B and Ref. [4]) for ideal polymers (where $F^{\text{ex}}=0$) by

$$\rho_s^{\mathrm{mid}}(\mathbf{r}) = \exp\{-\beta[V^{\mathrm{ext}}(\mathbf{r})/n - \mu]\}[G^{\mathrm{lin}}_{(n-1)/2}(\mathbf{r})]^2, \quad (7)$$

where the propagators, $G_j^{\mathrm{lin}}(\mathbf{r})$, for freely jointed chains are given by

$$G_j^{\mathrm{lin}}(\mathbf{r}_1) = \int d\mathbf{r}_2 G_{j-1}^{\mathrm{lin}}(\mathbf{r}_2)\exp[-\beta V^{\mathrm{ext}}(\mathbf{r}_2)/n] \times \exp(-n\beta\lambda r_{12}^2), \quad j > 0,$$

$$G_0^{\mathrm{lin}}(\mathbf{r}_1) = 1. \quad (8)$$

Here, μ is the Lagrange multiplier that achieves the correct total number of middle-sites (which becomes the configurational contribution to the chemical potential in the grand canonical ensemble). Note that in their work [4] Broukhno *et al.* use the index "$n/2$" in Eq. (7) and consider polymers with an even number of sites, instead of the index "$(n-1)/2$" and polymers with an odd number of sites. It follows that the external potential in their work is too large by a factor of $(1+n^{-1})$. This will reduce the rate of convergence as $n \to \infty$ in their work, and explains why large values of n are needed in their work even for high temperatures. For nonideal ring polymers (where the excess functional $F^{\mathrm{ex}} \neq 0$), the external potential $V^{\mathrm{ext}}(\mathbf{r})$ in Eqs. (7) and (8) is replaced by $V^{\mathrm{ext}}(\mathbf{r}) + \delta F^{\mathrm{ex}}/\delta\rho(\mathbf{r})$, where $\rho(r) = \rho_s^{\mathrm{mid}}(r)$. This excess functional is defined later.

However, contrary to their claims, the ORA does not become exact in the limit $n \to \infty$. It is well known that the statistics of fully flexible noninteracting ring and chain polymers are very different [6,7], and in the $n \to \infty$ limit the squared radius of gyration for a ring polymer is half that of a chain polymer. Because the density profile of the middle site in a chain polymer is influenced by the distribution of the other sites in the same polymer, this implies that it cannot be equivalent to the density profile of a site in a ring polymer. One can also compare the total intrapolymer site-site pair correlation function for the middle site in a chain polymer and any site in the corresponding ring polymer in the $n \to \infty$ limit for a bulk situation. Figure 1 clearly shows that these polymers are quite different (see Appendix B for a derivation of the equations depicted in Fig. 1). This figure compares these functions for $n = 1001$, which is sufficiently large that no visible difference is observed on the scale of this plot when n is increased further. The ring polymer is much more compact than the chain polymer. This means that we should expect the chain polymer to underpredict the true density profile of a quantum system in the grand canonical ensemble because it will tend to generate too much smoothing due to dispersion. The effect for a canonical ensemble system will be more subtle because the total number of particles is fixed. However, we still should expect it to produce a smoother, more dispersed, density profile.

So in general we should not expect the ORA to be accurate. Yet in their work, Broukhno *et al.* showed that it was extremely accurate for some particular spherically symmetric external potentials, namely the 3D-QHO and for the electron density surrounding some atomic nuclei. They claim that this level of accuracy should also be seen more generally. One of the aims of this present work is to show that this is not the case.

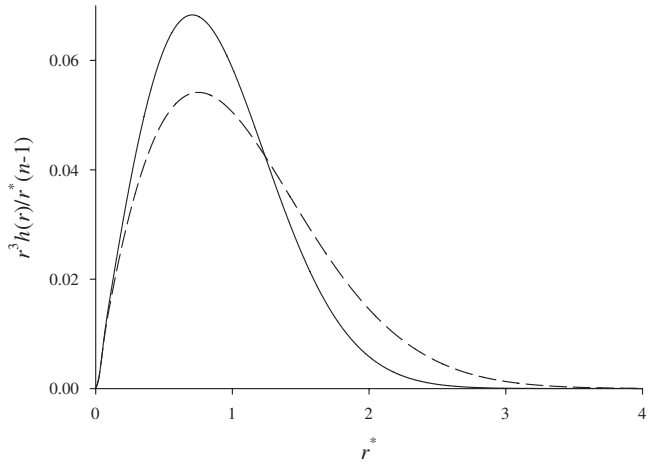

FIG. 1. Comparison of the normalized total site-site intramolecular correlation function for fully flexible noninteracting chain (dashed line) and ring polymers (full line) in the limit $n \to \infty$. For the chain polymer this function is evaluated with respect to the middle site of a polymer with an odd number of sites, while for the ring polymer this function is identical for each site. The reduced radius $r^* = r\sqrt{4\beta\lambda}$.

B. Feynman-Hibbs technique

In this approach a quantum particle is approximated by a three-dimensional Gaussian wave packet which is used to calculate effective interactions between the quantum particle and other particles. It is a well-known technique that is described in detail elsewhere [1,24,25]. The effective potential is

$$V_{\mathrm{cl}}^{\mathrm{eff}}(\mathbf{r}_1) = (2\pi\Delta q^2)^{-3/2} \int d\mathbf{r}_2 V^{\mathrm{cl}}(\mathbf{r}_2)\exp(-r_{12}^2/2\Delta q^2), \quad (9)$$

where $\Delta q^2 = \beta\hbar^2/12m = k_B T/24\lambda$, $r_{12} = |\mathbf{r}_1 - \mathbf{r}_2|$, V^{cl} is the "bare" classical potential, and the mass m is the reduced mass of the quantum particle and the object it is interacting with. Although it is straightforward to evaluate this integral precisely numerically, for some of the divergent potentials used in this work it should approximated by performing a Taylor series expansion of the interaction potential V^{cl} about $\mathbf{r}_1$. For the effective interaction between two spherical quantum particles the result to second order in the series expansion is

$$\phi^{\mathrm{eff}}(r) = \phi(r) + \left(\frac{\beta\hbar^2}{24m}\right)\nabla^2\phi(r) = \phi(r) + \left(\frac{\beta\hbar^2}{12m}\right)\left(\frac{\partial^2\phi(r)}{\partial r^2} + \frac{2}{r}\frac{\partial\phi(r)}{\partial r}\right), \quad (10)$$

where r is their separation and m is the mass of one particle. For the effective interaction between a quantum particle and an immobile spherically symmetric external potential the corresponding result is

$$V_{\text{ext}}^{\text{eff}}(r) = V^{\text{ext}}(r) + \left(\frac{\beta\hbar^2}{24m}\right)\nabla^2 V^{\text{ext}}(r)$$
$$= V^{\text{ext}}(r) + \left(\frac{\beta\hbar^2}{24m}\right)\left(\frac{\partial^2 V^{\text{ext}}(r)}{\partial r^2} + \frac{2}{r}\frac{\partial V^{\text{ext}}(r)}{\partial r}\right). \tag{11}$$

For the effective interaction between a quantum particle and an immobile planar surface the result is

$$V_{\text{ext}}^{\text{eff}}(z) = V^{\text{ext}}(z) + \left(\frac{\beta\hbar^2}{24m}\right)\frac{\partial^2 V^{\text{ext}}(z)}{\partial z^2}, \tag{12}$$

where z is the distance normal to the surface. These effective interaction potentials can be combined with DFT for classical fluids to arrive at an Euler-Lagrange equation for the density profile of the effective classical particles,

$$\rho^{\text{eff}}(\mathbf{r}_1) = \exp\left[-\beta\left(V_{\text{ext}}^{\text{eff}}(\mathbf{r}_1) - \mu + \frac{\delta F^{\text{ex}}}{\delta\rho^{\text{eff}}(\mathbf{r}_1)}\right)\right], \tag{13}$$

where μ is the Lagrange multiplier (or configurational chemical potential for the grand canonical ensemble) and F^{ex} is an excess Helmholtz free-energy density functional for a system described in terms of effective interactions, ϕ^{eff}. These interactions and the corresponding F^{ex} are described in the next section. To obtain the actual density profile including the effect of quantum dispersion the effective density profile must be convoluted with the 3D wavepacket once more. So we have

$$\rho(\mathbf{r}_1) = (2\pi\Delta q^2)^{-3/2}\int d\mathbf{r}_2\rho^{\text{eff}}(\mathbf{r}_2)\exp(-r_{12}^2/2\Delta q^2). \tag{14}$$

This technique is denoted FH-DFT.

C. Excess functional

Each of the techniques described above requires a prescription for the excess functional. In this work an excess functional is only needed for the hydrogen physisorption problem since the 3D QHO test only involves a single particle. If our system comprises only ring polymers representing hydrogen molecules, and if we label the sites on each ring polymer $1\ldots n$ and consider the system to consist of a mixture of sites, i.e., if we adopt the interaction-site model of Chandler *et al.* [22,23] (6), then the excess functional for a grand canonical ensemble can be written using the well-known density functional relation [26]

$$F^{\text{ex}} = k_B T\sum_{ij=1}^{n}\int_0^1 d\alpha(\alpha-1)\int d\mathbf{r}_1\int d\mathbf{r}_2\rho_i(\mathbf{r}_1)\rho_j(\mathbf{r}_2)$$
$$\times c_{ij,\text{ex}}^{(2)}(\mathbf{r}_1,\mathbf{r}_2,\rho_\alpha), \tag{15}$$

where $c_{ij,\text{ex}}^{(2)}(\mathbf{r}_1,\mathbf{r}_2,\rho_\alpha)$ is the "excess" pair-direct correlation function acting between sites i and j for the system with density $\rho_\alpha=\alpha\rho(\mathbf{r})$ and $\rho_i(\mathbf{r})$ is the density of sites labeled i. This excess function is simply the total site-site pair-direct correlation function less the contribution due to the bonding functional $c_{ij,\text{ex}}^{(2)}(\mathbf{r}_1,\mathbf{r}_2)=c_{ij}^{(2)}(\mathbf{r}_1,\mathbf{r}_2)-c_{ij,b}^{(2)}(\mathbf{r}_1,\mathbf{r}_2)$, where $c_{ij,b}^{(2)}(\mathbf{r}_1,\mathbf{r}_2)=-\beta\delta^2F^b/\delta\rho_i(\mathbf{r}_1)\delta\rho_j(\mathbf{r}_2)$. Because of the symmetry of the ring and because each site is identical (except for its label), Eq. (15) can be written

$$F^{\text{ex}} = k_B T\int_0^1 d\alpha(\alpha-1)\int d\mathbf{r}_1\int d\mathbf{r}_2\rho(\mathbf{r}_1)\rho(\mathbf{r}_2)c_n^{(2)}(\mathbf{r}_1,\mathbf{r}_2,\rho_\alpha), \tag{16}$$

where $c_n^{(2)}=n\Sigma_{j=1,n}c_{1j,\text{ex}}^{(2)}$. Because there are no site labels in Eq. (16), it has the same form as a density functional theory for a simple classical system interacting via an effective ring-polymer–ring-polymer interaction that generates the pair-direct correlation function $c_n^{(2)}$. The Feynman-Hibbs technique prescribes an approximation for this effective interaction via Eq. (10). But in general we are free to choose the effective interaction so that it generates these pair correlations accurately. Density functionals able to model these effective interactions are discussed below. As mentioned earlier in the context of the ORA technique, the external potential, $V^{\text{ext}}(\mathbf{r})$, in Eqs. (7) and (8) should be replaced with $V^{\text{ext}}(\mathbf{r})+\delta F^{\text{ex}}/\delta\rho(\mathbf{r})$, where F^{ex} is given by Eq. (16). We denote this technique ORA-DFT. But note that the derivation of F^{ex} here is quite general, and not limited to the ORA-based method.

In this work molecular hydrogen is modeled as a single quantum particle and the distinction between ortho- and parahydrogen is not made. This model is thought to be sufficient at the temperatures considered in this work. So, for both the FH-DFT and ORA-DFT techniques we must define an excess functional corresponding to a model of effective H_2-H_2 interactions. In this work all such effective interactions are described by Lennard-Jones (LJ) interactions and hence standard excess functionals that describe LJ fluids are used. Although the FH technique actually prescribes a slightly different effective interaction, this effective FH interaction is accurately modelled by a LJ interaction (see the Results section). So a standard approximate DFT expression for LJ fluids is used

$$F^{\text{ex}}[\rho(\mathbf{r})] = F_d^{\text{ex}}[\rho(\mathbf{r})] + \frac{1}{2}\int d\mathbf{r}_1\int d\mathbf{r}_2\rho(\mathbf{r}_1)\rho(\mathbf{r}_2)\phi_{\text{att}}(\mathbf{r}_{12}), \tag{17}$$

where F_d^{ex} is the original fundamental measure hard-sphere functional of Rosenfeld [27] and of Kierlik and Rosinberg [28,29], and ϕ_{att} is the attractive contribution to LJ interaction. The hard-sphere diameter d is set equal to the LJ length parameter σ^{eff}, while ϕ_{att} is determined according to the prescription of Weeks, Chandler, and Andersen (WCA) [30] applied to a cut-and-shifted LJ potential

$$\phi_{\text{att}}(r) = \begin{cases} -\varepsilon^{\text{eff}} - \phi_{\text{LJ}}(r_c), & r \leqslant 2^{1/6}\sigma^{\text{eff}}, \\ \phi_{\text{LJ}}(r) - \phi_{\text{LJ}}(r_c), & 2^{1/6}\sigma^{\text{eff}} < r \leqslant r_c, \\ 0, & r > r_c, \end{cases} \tag{18}$$

where ϕ_{LJ} is the Lennard-Jones model

$$\phi_{\mathrm{LJ}}(r) = 4\varepsilon^{\mathrm{eff}}(x^{-12} - x^{-6}), \tag{19}$$

$x = r/\sigma^{\mathrm{eff}}$, and r_c is the cutoff radius (equal to 1.5 nm in this work). These functionals are well known and described elsewhere in detail [26]. Application to slit pores is straightforward [31,32]. Although other potentials thought to be more accurate have been used to model molecular hydrogen in other work they are not used here for several reasons. First, the focus of this work is not actually the precise prediction of hydrogen adsorption, but instead the comparison of several techniques capable of modelling hydrogen adsorption efficiently. On this basis alone there is no need to use models that might offer slightly greater accuracy than the LJ model, which is adequate for the purpose of this work. Secondly, it is likely that the approximation (17), which could be applied straightforwardly to other potentials if required to do so, generates greater error than choosing the LJ potential over other possibly more accurate potentials. In any case, we will see below that the LJ potential and Eq. (17) is able to accurately reproduce a bulk isotherm of hydrogen at 77 K.

As mentioned above, this excess density functional prescription for LJ fluids is known [33,34] to be only reasonably accurate for modelling adsorbed fluids, even if the model parameters are chosen to accurately reproduce bulk data. Much greater accuracy can often be achieved [33,34] with more sophisticated (and somewhat more demanding) density functionals for LJ fluids.

Both the FH-DFT and ORA-DFT techniques are solved by Picard iteration. The excess density functional is given in each case by Eq. (17), but the effective Lennard-Jones parameters that enter this functional are different in the FH-DFT and ORA-DFT approaches and determined later.

D. PI-MC simulations

The techniques described above based on classical density functionals are compared to results generated by PI-MC. Canonical ensemble PI-MC simulation is used for the 3D-QHO test, while the grand canonical PI-MC technique (PI-GCMC) used in this work to model hydrogen adsorption is similar to that introduced by Wang and Johnson [35]. The only significant difference with their work is that a hybrid MD technique is not used to perform a displacement move. Instead, a more straightforward Monte Carlo scheme is used. In this scheme a trial displacement consists of moving a single ring-polymer as follows. Each site on the ring-polymer is moved by the same amount $\mathbf{dr}_0$ (chosen randomly with uniform probability from within a sphere of radius dr_0), and then each site is also moved an additional $\mathbf{dr_i}$ (chosen randomly with uniform probability within a sphere with radius dr_1), where $\mathbf{dr_i}$ is different for each site i. $dr_1 < dr_0$ must be quite small to ensure a reasonable probability of acceptance (generally about 50%). For each simulation 5.12 million trial moves are attempted, half of which are attempted displacement moves (the other half are trial insertions and deletions), with an additional 0.5 million attempts to allow equilibration. 100 noninteracting "gas-phase" PI ring polymers are simulated simultaneously to provide a pool of random configurations that can be used to generate trial insertions. This PI-GCMC technique is compared with exact results for the 3D QHO to determine the largest value of n for which it is ergodic for the kinds of systems studied here. Results are presented later.

E. Test systems

The 3D QHO system is studied to confirm the results of Broukhno *et al.* for the ORA and to validate the PI-GCMC algorithm used here. A 3D harmonic oscillator is defined by the potential

$$V^{\mathrm{ext}}(r) = \frac{1}{2}Kr^2, \tag{20}$$

where K is the spring constant. We consider a single quantum particle system at fixed temperature, i.e., a canonical ensemble. The exact solution for energy levels and density profiles of the 3D QHO is given in Appendix A. From this solution we see that only two independent parameters are needed to define a 3D QHO: An inverse length

$$\gamma = \sqrt{\sqrt{Km}/\hbar} \tag{21}$$

and the dimensionless parameter

$$\delta = \frac{\hbar\sqrt{K/m}}{k_B T}, \tag{22}$$

which is related to the probability that the system is in its ground state, $p(0) = [2e^{-\delta/2}\sinh(\delta/2)]^3$. So, by working with a reduced length, $r^* = r\gamma$, we have to consider only one parameter, δ. Because of the spherical symmetry of this potential numerical solutions are most conveniently found using fast Fourier transforms [31].

The main part of this paper studies hydrogen physisorption at low temperature. For this problem the bare, or high temperature, hydrogen molecule–hydrogen molecule interaction (i.e., not the effective hydrogen molecule–hydrogen molecule interaction) is set equal to that used in other work [11]. That is, a molecular hydrogen site is modeled as a Lennard-Jones particle with energy and length parameters equal to $\varepsilon_{\mathrm{ff}}/k_B = 36.7$ and $\sigma_{\mathrm{ff}} = 0.296$ nm, respectively. As usual, a slit-pore is defined as two parallel ideal walls separated by a distance H

$$V^{\mathrm{ext}}(z) = V^{\mathrm{st}}(z) + V^{\mathrm{st}}(H - z), \tag{23}$$

where the hydrogen molecule–graphitic wall interaction is provided by the Steele potential [31]

$$V^{\mathrm{st}}(z) = 2\pi\rho_s\Delta\sigma_{sf}^2\varepsilon_{sf}\left[\frac{2}{5}\left(\frac{\sigma_{sf}}{z}\right)^{10} - \left(\frac{\sigma_{sf}}{z}\right)^4 - \frac{\sigma_{sf}^4}{3\Delta(0.61\Delta + z)^3}\right] \tag{24}$$

and the Lorentz-Berthelot mixing rules are used to define cross parameters

$$\sigma_{sf} = (\sigma_{ff} + \sigma_{ss})/2, \quad \varepsilon_{sf} = \sqrt{\varepsilon_{ff}\varepsilon_{ss}}. \tag{25}$$

Surface parameters appropriate for modeling graphite are [31] $\varepsilon_{\mathrm{ss}}/k_B = 28.0$ K, $\sigma_{\mathrm{ss}} = 0.34$ nm, $\rho_s = 114$ nm^{-3}, and $\Delta = 0.335$ nm.

III. RESULTS

A. 3D-QHO

Let us consider the Feynman-Hibbs technique applied to the 3D-QHO first. Application of Eqs. (9)–(20) gives the well-known [24] result

$$V_{\mathrm{ext}}^{\mathrm{eff}}(r) = V^{\mathrm{ext}}(r) + \frac{3K}{2}\Delta q^2. \tag{26}$$

Essentially, the entire potential is shifted by a constant amount. The same result is obtained using the second order version (11). In this system, for which the number of particles is fixed at one, this shift of the potential will have no effect on the density profile of the effective classical particles; it will be exactly the same as the classical result. The effect of quantum dispersion on the density profile is included through Eq. (14), giving the result

$$\rho(r) = \left(\frac{\beta K \eta}{2\pi}\right)^{3/2} e^{-(\beta K \eta/2)r^2}, \tag{27}$$

where $\eta=(K\Delta q^2+1)^{-1}$. Likewise, the average energy is increased above the classical energy by $3K\Delta q^2/2$. These results are displayed in Figs. 2(a) and 2(b) (density profiles) and Table I (energies), where they are compared with exact results (A4), and results from the ORA. The ORA results of Broukhno *et al.* for this system are reproduced, albeit much more efficiently than in their work, due to the use of the correct ORA expression (7).

Figure 2(a) compares results for the density profile when $\delta=8$ [corresponding to $p(0)=0.999$], where r^* is described above and $\rho^*=\rho/\gamma^3$ is the reduced particle density with respect to this reduced length scale. The main plot shows that the ORA performs exceptionally well in this case. Using the ORA, results for $n\sim 81$ and above cannot be distinguished from exact results on the scale of this plot. The FH result significantly "oversmooths" the density profile, which is expected because the Gaussian wave packet employed is fixed in this approximation and cannot adjust to the presence of the external potential.

Figure 2(b) is similar to Fig. 2(a) except that the temperature is higher [$\delta=1$, corresponding to $p(0)=0.253$]. Similar comments apply, except now the FH result is much more accurate at this higher temperature. Because the correct ORA expression (7) is used in this work it generates satisfactory results even for $n=11$, which is several orders of magnitude smaller than typical values in Ref. [4].

Table I displays the energy for each result shown in Figs. 2(a) and 2(b). For each approximate calculation the total energy is determined from the average potential energy via the virial theorem [36], which in this particular case is

$$2\langle E_{\mathrm{kin}}\rangle = \left\langle r\frac{\partial V^{\mathrm{ext}}}{\partial r}\right\rangle. \tag{28}$$

Here, E_{kin}. is the kinetic energy and the angle brackets denote an ensemble average. For the classical and FH approaches $E_{\mathrm{kin}}=3k_BT/2$, and hence the total energy is easily calculated. For the ORA approach the right-hand term in Eq. (28) is simply twice the average potential energy. So the total energy is just twice the average potential energy, which is easily calculated from the density profile. The total energy for the exact result is given in Appendix A. Note that if the energy for each technique had been calculated from the resulting approximate wave function and the Schrödinger equation then each result in Table I would be greater than 1, since 1 indicates the ground state. But this is clearly incorrect for a classical system; hence the use of the virial theorem in

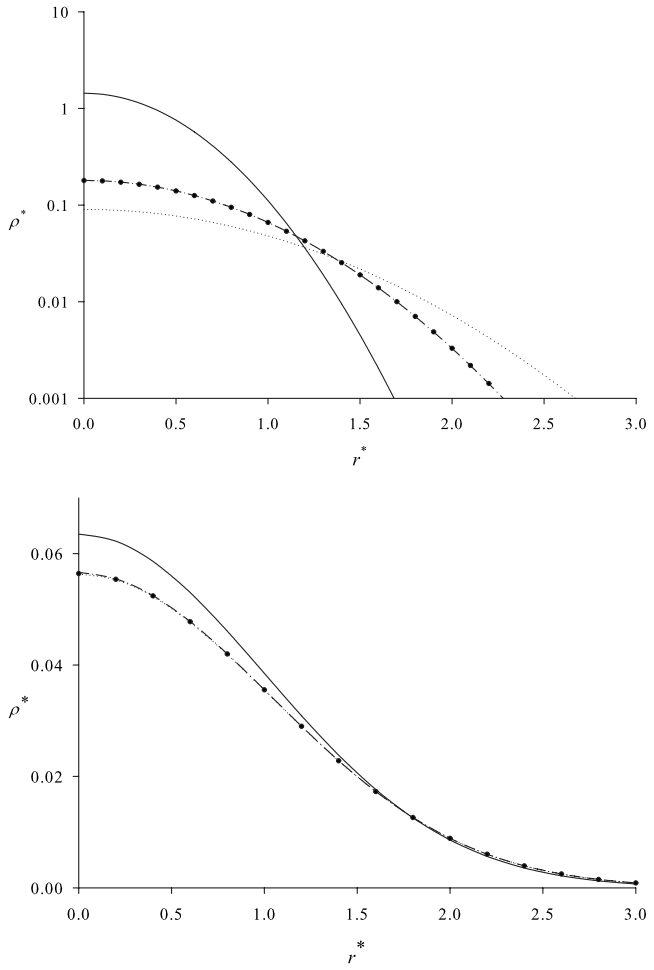

FIG. 2. (a) Density profiles for the 3D QHO with $\delta=8$. The circles are exact quantum results, while the solid line is the exact classical result. The dot-dash and dottted lines are results from the ORA (with $n=81$) and the FH methods, respectively. The reduced length and density are r^* and ρ^*, respectively. The reduced density is shown on a logarithmic scale. (b) As for (a) except that $\delta=1$, for the ORA result $n=11$, and reduced density is shown on a linear scale.

TABLE I. The total energy of the 3D-QHO predicted by several methods, expressed relative to the ground-state energy, where δ is given by Eq. (22).

δ	Exact	ORA	FH	Classical
8	1.0007	0.9995	0.9167	0.25
1	2.164	2.162	2.083	2.0

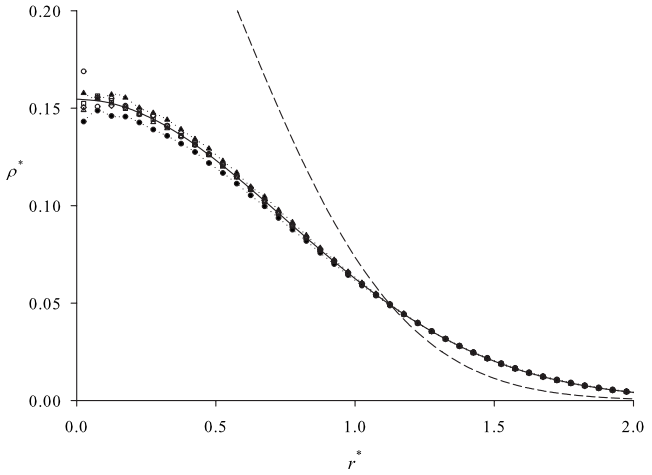

FIG. 3. PI-GCMC results using the algorithm described in the text for the 3D-QHO with $\delta=3$ using a range of values of n: $n=8$ (solid triangles with dashed line), $n=12$ (open circles), $n=16$ (open squares), $n=20$ (open diamonds), $n=24$ (open triangles), and $n=28$ (solid circles with dashed line). The dashed line is the classical result while the solid line is the exact quantum result. The reduced length and density are r^* and ρ^*, respectively. Statistical errors are usually smaller than symbols sizes, except for a few points close to the origin.

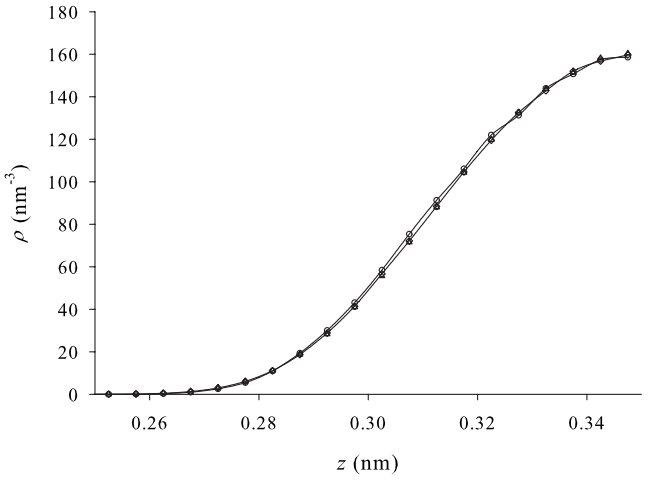

FIG. 4. PI-GCMC results for hydrogen adsorption in a 0.7 nm graphitic slit pore at 77 K and $\xi=1.0$ using a range of values of n: $n=4$ (open circles), $n=8$ (open diamonds), and $n=12$ (open triangles). Lines are a guide to the eye and statistical errors are smaller than symbols sizes. Only a left-hand portion of the pore is shown; z is the distance from the left-hand pore wall.

this work and in Ref. [4] which is appropriate for techniques based on ring-polymer models.

Finally, the PI-GCMC algorithm is tested to determine the range of n over which it is ergodic for $\delta=3$. This value of δ is chosen because it produces a similar degree of quantum dispersion to the hydrogen adsorption problem at 77 K, and so is a suitable validation test of the PI-GCMC algorithm used here. The grand-canonical technique is tested using noninteracting quantum particles. An arbitrary chemical potential is chosen, and the final density is scaled to achieve an average of 1 particle in the 3D-QHO.

Figure 3 shows PI-MC results for several values of n, and compares them against exact classical and quantum results. By inspection, we see that $n \geqslant 12$ is sufficient for this system, but the technique starts to become nonergodic for $n > 24$.

B. Hydrogen physisorption in graphitic pores

Each of the above techniques are compared for a model of hydrogen adsorption in graphitic pores at 77 K, which roughly corresponds to the lower bound of interest in hydrogen physisorption studies. Pores of 0.7 nm and 2 nm in width are considered because they represent quite different situations. When $H=0.7$ nm only a single layer of hydrogen is adsorbed, while for $H=2.0$ nm we have a layer of hydrogen on each wall with much more dilute gas filling the remainder of the pore.

The first task is to determine the lowest value of n that is sufficient in the PI-GCMC simulations to obtain accurate results. A demanding scenario here is the 0.7 nm pore at the highest activity $\xi=\rho_b \exp(\beta\mu^{\mathrm{ex}})$. Figure 4 displays PI-GCMC results for several values of n at 77 K and $\xi=1.0$ in this pore. We see that increasing n beyond 8 has little impact relative to the statistical error in the results. So for all other PI-MC simulations at 77 K n is set to 12, which by comparison with the $\delta=3$ 3D-QHO results in Fig. 3 is thought to be well within the ergodic regime. Wang and Johnson [18] find that $n=15$ is sufficient in their work at 77 K.

The effective FH potential calculated from Eq. (11) is shown in Fig. 5. For convenience a LJ potential is used in place of the effective FH potential. Figure 5 also shows this effective FH LJ potential which is determined by finding the closest fit to the second moment of the Mayer function [37] (which ensures close agreement in the second virial coefficient). So, the effective LJ parameters used for the FH technique are $\sigma^{\mathrm{eff}}=0.3076$ nm and $\varepsilon^{\mathrm{eff}}/k_B=31.62$ K at 77 K.

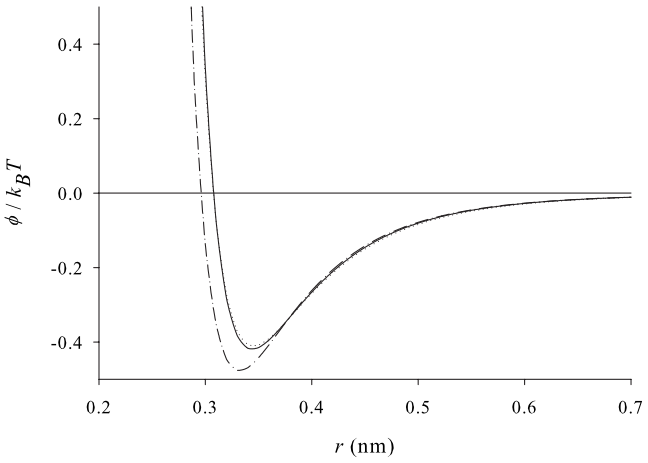

FIG. 5. Molecular hydrogen–molecular hydrogen interactions used in this study. The full line is the Feynman-Hibbs interaction resulting from operating on the site-site potential (dashed-dot line) via Eq. (10). The dotted line is the best Lennard-Jones interaction that fits this FH interaction with respect to the second virial coefficient.

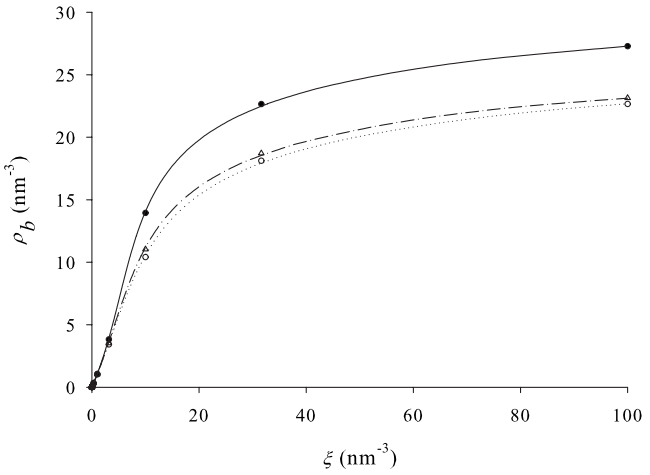

FIG. 6. Bulk isotherms for models of molecular hydrogen at 77 K. The solid circles are classical GCMC results using the bare hydrogen molecule–hydrogen molecule potential and the solid line corresponds to the best fit to them using the DFT (17) with parameters in Table II. The open circles are PI-GCMC results, and the dotted line corresponds to the best fit to them using the ORA-DFT with parameters in Table II. The open triangles are GCMC results using the FH-LJ potential shown in Fig. 5, and the dashed-dotted line corresponds to the best fit to them using the FH-DFT with parameters in Table II.

Next, the effective LJ parameters for the FH-DFT and ORA-DFT techniques are determined. For the ORA-DFT technique the effective LJ parameters are optimized to reproduce bulk hydrogen isotherms generated by PI-MC simulations. Here, the aim is to produce the smallest root-mean-square deviation between the bulk isotherm generated by simulation and the bulk isotherm generated by the bulk limit of the DFT. This idea is similar to that used by Kowalczyk and MacElroy [21] in their application to bulk thermodynamics of hydrogen. The best fit DFT parameters to the PI-GCMC results are found to be $\sigma^{\text{eff}}=0.2903$ nm and $\varepsilon^{\text{eff}}/k_B=28.10$ K, while the best fit DFT parameters to GCMC simulations of the LJ potential which is fitted to the FH potential in Figure 5 are $\sigma^{\text{eff}}=0.2908$ nm and $\varepsilon^{\text{eff}}/k_B=29.60$ K. To compare with classical results the same LJ parameter fitting process is used, where this time the best fit is found to classical GCMC simulations results. This gives $\sigma^{\text{eff}}=0.281$ nm and $\varepsilon^{\text{eff}}/k_B=34.30$ K. Each bulk isotherm is shown in Fig. 6. All these effective interaction parameters are summarized in Table II. The effective FH external potential corresponding to the interaction of hydrogen with a pore wall is obtained by combining Eqs. (23) and (24) with Eq. (12).

One advantage of generating effective hydrogen model parameters via this calibration method is that an effective LJ model for hydrogen can be found that compensates, to a degree, for the inaccuracy of the excess functional (17). Although it could be argued that this method is computationally demanding, because GCMC or PI-GCMC simulations are used to generate the reference bulk isotherms, this would not be the case when using experimental data rather than simulation data as a reference, which would normally be the case.

TABLE II. Effective Lennard-Jones parameters used in this study. The FH-LJ parameters are found by fitting a Lennard-Jones potential to the true FH potential obtained via Eq. (10). The other parameters are obtained by fitting a bulk isotherm generated by the respective DFT to a bulk isotherm generated by MC simulation (PI-GCMC for the ORA-DFT method).

δ	FH-LJ	FH-DFT	ORA-DFT	DFT
σ^{eff} (nm)	0.3076	0.2908	0.2903	0.2810
$\varepsilon^{\text{eff}}/k_{\text{B}}$ (K)	31.62	28.60	28.10	34.30

Note that the resulting effective hydrogen–hydrogen LJ interaction parameters are quite similar for the FH-DFT and ORA-DFT techniques, and σ^{eff} is slightly larger than for the corresponding classical parameters, as expected. However, these results are very different to the effective LJ parameters obtained by Kowalczyk and MacElroy [21] for hydrogen at 77 K. They find σ^{eff} to be much smaller (0.240 nm or 0.207 nm depending on the pressure range) than the corresponding parameter of the bare hydrogen interaction (0.296 nm), which is unexpected and suggests that there might be an error in their calculations.

Now that all model parameters have been calibrated we can begin to compare the performance of each technique. First, the 77 K isotherms for the ORA-DFT and FH-DFT techniques are compared with simulation results for the 2.0 nm pore in Fig. 7(a). Note that the FH-DFT density profile is obtained from Eq. (14). Also shown in Fig. 7(a) are the corresponding classical results. Results are presented in terms of the average pore density

$$\rho_{\text{av}} = \frac{1}{H}\int_0^H dz\, \rho(z) \tag{29}$$

as a function of the bulk density. Figure 6 can be used to convert bulk density to the activity ξ. We see that the classical simulation and DFT results agree well at low bulk density, which is to be expected because at low density the excess functional, which is known to not be very accurate, plays an insignificant role. As the bulk density increases the excess functional becomes more significant and so the agreement deteriorates, even though the Lennard-Jones parameters input to this classical DFT have been calibrated to reproduce the bulk MC simulation isotherm. "Switching on" quantum fluctuations generates the PI-GCMC simulation, ORA-DFT and FH-DFT results. We see good agreement at low bulk density between the PI-GCMC and FH-DFT results, but the FH-DFT results deteriorate at higher bulk densities. Note that the FH-DFT isotherm, relative to the PI-GCMC isotherm, exhibits similar behaviour to the classical DFT isotherm, relative to the GCMC results, as bulk density increases. This indicates that it is the excess functional, both in the classical DFT and FH-DFT cases, that is generating this error. Conversely, the ORA-DFT result is relatively poor at low bulk density, where the excess functional is insignificant. This happens because the ORA generates too much smoothing of the density profile. However, at higher bulk densities agreement between PI-GCMC and the ORA-DFT improves.

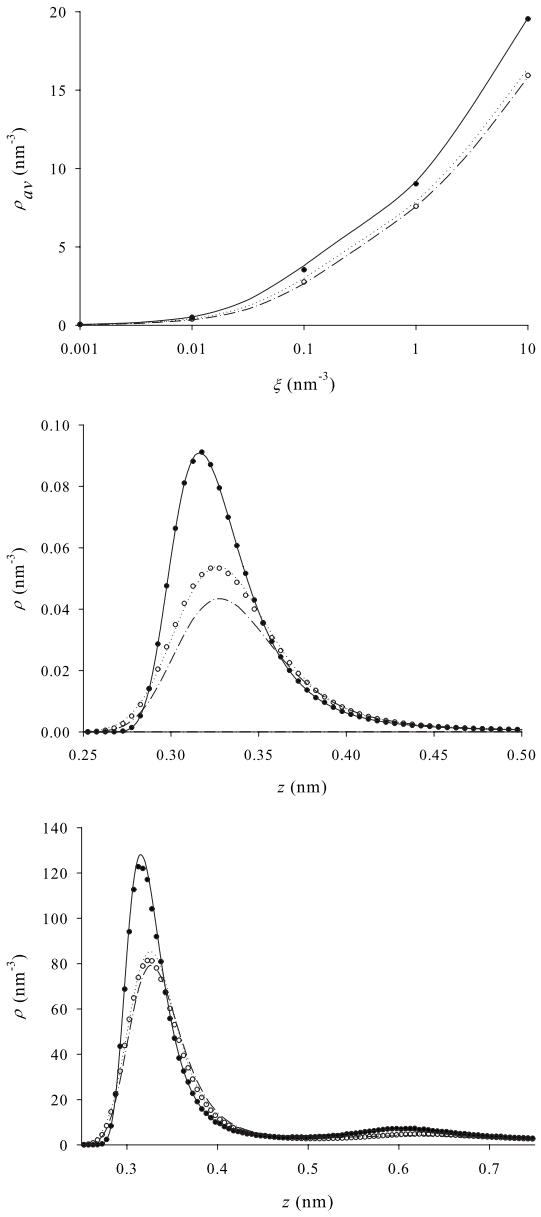

FIG. 7. (a) Average pore density isotherms for hydrogen at 77 K in a 2.0 nm graphitic pore predicted by each technique: Classical GCMC (solid circles), PI-GCMC (open circles), classical DFT (solid line), FH-DFT (dotted line), and ORA-DFT (dot-dashed line). Statistical errors are smaller than symbol sizes. The activity ξ is on a logarithmic scale. (b) Density profiles for hydrogen at $\xi = 0.0001$ nm^{-3} and 77 K in a 2.0 nm graphitic slit pore predicted by each technique: Classical GCMC (solid circles), PI-GCMC (open circles), classical DFT (solid line), FH-DFT (dotted line), and ORA-DFT (dot-dashed line). For clarity, only a portion of the density profile is shown 0.25 nm$<z<$0.5 nm. (c) As for (b) except $\xi = 1.0$ nm^{-3} and only the portion 0.25 nm$<z<$0.75 nm is shown.

This is because of a fortuitous cancellation of errors; the simple DFT used here cancels some of the error inherent in the ORA.

Figures 7(b) and 7(c) provide more insight into this behaviour. Figure 7(b) shows a portion of the density profiles corresponding to $\xi = 0.0001$ nm^{-3}, while Fig. 7(c) shows the density profiles corresponding to $\xi = 1.0$ nm^{-3}. The effect of including quantum fluctuations is clear; the height of the peak signifying the first adsorbed layer is significantly reduced, to nearly half its classical value. At $\xi = 0.0001$ nm^{-3} we see excellent agreement between classical MC simulation and DFT, which must agree perfectly in the low density limit. We also see rather good agreement between the PI-GCMC and FH-DFT results. In contrast, the ORA-DFT density profile is quite poor due to excessive smoothing. However, at $\xi = 1.0$ both the FH-DFT and ORA-DFT results are in reasonable agreement with PI-GCMC results. This change in the accuracy of each method is a reflection of the accuracy of the DFT used for F^{ex}.

Similar behavior is observed for the 0.7 nm pore. Figure 8(a) shows the corresponding average pore density isotherm, while Figs. 8(b) and 8(c) display portions of the density profiles corresponding to $\xi = 0.000\,001$ and $\xi = 1.0$. Note that for both the 2.0 nm and 0.7 nm pores the average pore density is reduced relative to the classical result by over 20% at moderate densities, while the peak height in the density profile is reduced by about 40% for the 2.0 nm pore.

If we compare results of Gu *et al.* published in Ref. [11] with those here we see that both the PI-DFT and PI-GCMC results in Ref. [11] are qualitatively incorrect for low bulk densities. In particular, in Figs. 2a, 3a, and 4a in Ref. [11] we see the effect of including quantum dispersion at 100 and 70 K, relative to the classical result, is very significant. The density peak corresponding to the first adsorbed layer appears to be dramatically reduced, although admittedly the entire classical profile is not reproduced in these figures. This behaviour is qualitatively different to that observed here where the effect of quantum dispersion is much more modest at 77 K. Although these results in Ref. [11] correspond to cylindrical pores, which model carbon nanotubes, and bulk densities in the range 3 to 5 nm^{-3}, these cylindrical pores are sufficiently wide that qualitative comparison with the 2.0 nm slit pore results at $\xi = 1.0$ here [Fig. 7(c)] is valid. Although we can expect the PI-DFT results in Ref. [11] to be poor (because of the SAFT-base ring-polymer model used), this does not explain why their PI-GCMC results agree with them.

IV. DISCUSSION

The aim of this work is to survey techniques based on classical density functionals able to model hydrogen physisorption at low temperature. Only methods able to treat quantum dispersion have been considered. In particular, techniques based on the ORA and FH approximations are compared at 77 K. To allow consideration of isotherms a density functional treatment of excess (hydrogen molecule–hydrogen molecule) interactions is developed for both techniques. We find that the FH technique is inherently more accurate than the ORA technique for this problem at low densities. This indicates that the fixed Gaussian wave packet representation of the quantum dispersion of molecular hydrogen at 77 K is accurate for adsorption in graphitic pores. However, the ORA technique is able to cancel some of the error inherent in the excess density functional at moderate and higher densi-

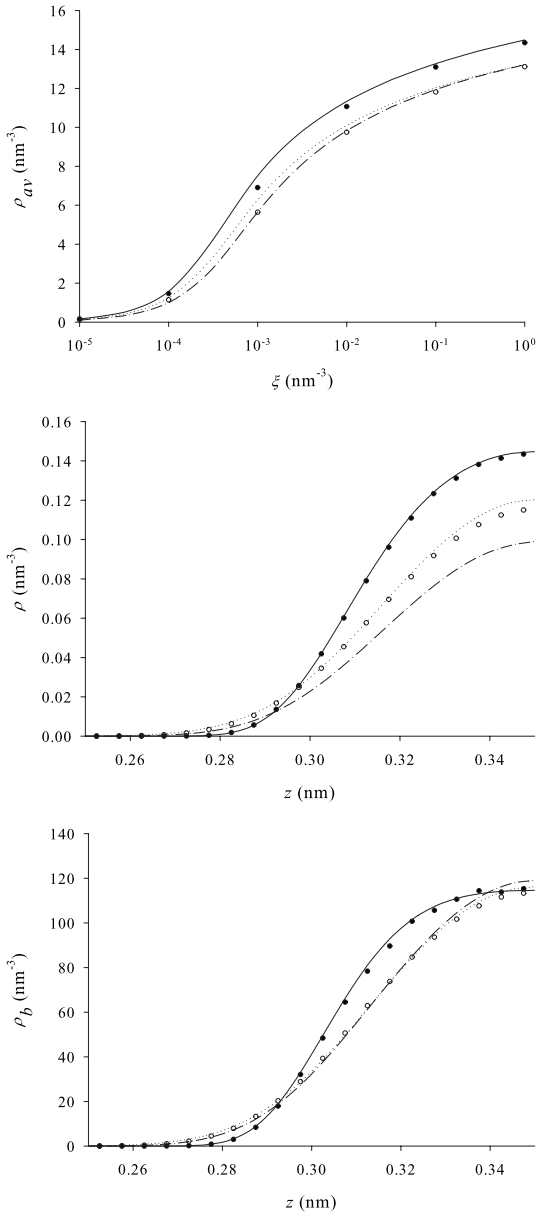

FIG. 8. (a) As for Fig. 7(a) except that the pore is 0.7 nm wide. (b) As for Fig. 7(b) except that the pore is 0.7 nm wide, $\xi = 0.000\,001$ nm^{-3} and only the portion 0.25 nm$< z <$0.35 nm is shown.(c) As for Fig. 8(b) except $\xi = 1.0$ nm^{-3}.

ties. This conclusion does not appear to depend on the slit pore width. So, the ORA-DFT technique is preferred overall unless more accurate density functionals are used to treat excess interactions. Existing density functionals [33,34] for Lennard-Jones fluids could be used in this context, but it is not yet clear whether they remain accurate in the narrowest pores. Unfortunately, the ORA-DFT technique is somewhat less efficient than the FH-DFT technique because of the additional numerical demand required to integrate the propagators, and this additional overhead increases linearly with n. Roughly, if the numerical effort required for the FH-DFT technique is proportional to $6+2r_c/d$, then the effort required for the ORA-DFT technique is $6+2r_c/d+(n-1)/2$, if each propagator integration is carried out on a mesh with the same number of points as (but a finer resolution than) the hard-sphere fundamental measure functional integrations. At much higher temperatures the ORA-DFT technique should become almost as efficient as the FH-DFT technique because it converges for smaller values of n at higher temperatures.

Each of these techniques could be applied to model hydrogen adsorption in real materials such as active carbons and carbon nanotubes, which are often [31,32] modeled in terms of slit or cylindrical pores. Because of the efficiency of each DFT technique, for which solutions are generally obtained in a matter of seconds on a desktop PC in this application to slit pores, they would be particularly suited to optimization studies of adsorption materials. In this case, the Lennard-Jones parameters could be calibrated by comparison with experimental data for bulk and adsorbed hydrogen rather than by comparison with PI-GCMC simulations. Note that the corresponding PI-MC simulations required tens of minutes to several hours, depending on the value of n, to obtain a satisfactory level of statistical error, which supports the view expressed in the introduction that DFT techniques can find useful applications.

It is interesting to try and understand why the ORA is remarkably accurate for the 3D-QHO problem as well as other central potentials. The problem with the ORA is that the statistics of a chain polymer are not the same as those of the corresponding ring polymer. This is because the end sites (with labels 1 and n) are not harmonically bonded as they are in a ring polymer. However, note that for a bulk fluid this final bond has no effect on the bulk density corresponding to a given chemical potential. Moreover, for problems involving attractive central potentials, like the 3D-QHO here and the hydrogen atom problem in Ref. [4], the average site 1–site n separation will reduce relative to its bulk value because of the constraining effect of the external potential. Indeed, this average separation will reduce as the confining external potential becomes stronger, so long as it is a central potential. Essentially, a confining central potential will, on average, "squeeze" these end sites together. This effect will not occur for other kinds of external potential. So, for attractive central potentials we can expect the statistics of chain polymers to converge to those of the corresponding ring polymers as the external potential becomes stronger. By interpolation then, because the ORA provides accurate density profiles for a uniform potential and for strongly attractive central potentials, we might also expect it to be accurate for any attractive central potential. For general potentials this is not the case; the ORA generates too much smoothing. Moreover, when the number of quantum particles is fixed, as with the application to the 3D-QHO and other central potential problems in Ref. [4], the Lagrange multiplier is chosen to ensure this constraint is satisfied. Essentially, the density profile is rescaled to satisfy this condition. This compensates to some degree for any inaccuracy in the ORA. This rescaling is not performed in grand canonical applications such as the hydrogen adsorption problem here, and so for this problem the error inherent in the ORA is more obvious.

Regarding other PI-DFT techniques based on classical density functionals, the method of Gu *et al.* [11] is shown to be qualitatively incorrect, while the weighted density approximation for bonding [13] can be extended to PI ring

polymers but requires calibration in advance, which is inconvenient.

Note that because quantum exchange is significant for *electrons* in atoms, molecules and solids the methods presented here cannot be applied immediately to model these particles. The most important missing ingredient is the exchange contribution to F^{ex} for electrons, i.e., the exchange functional. In principle, the same exchange-correlation functionals used with other electronic structure density functional techniques could be applied to the ORA-DFT method presented here. However, because of the limitations of the ORA we should only expect accurate results for central potential problems, e.g., the electronic structure of atoms and ions.

APPENDIX A: EXACT 3D QHO SOLUTIONS

For a single particle, exact solutions for the particle density are obtained by summing over the appropriately Boltzmann weighted distribution of quantum state densities. The 3D QHO can be treated as three independent orthogonal linear harmonic oscillators, so the particle density is

$$\rho(\mathbf{r}) = \frac{1}{Q}\sum_{n_x=0}^{\infty} \psi_{n_x}(x)\psi_{n_x}^*(x)\exp[-\beta\hbar\omega(n_x+0.5)] \times \frac{1}{Q}\sum_{n_y=0}^{\infty} \psi_{n_y}(y)\psi_{n_y}^*(y)\exp[-\beta\hbar\omega(n_y+0.5)] \times \frac{1}{Q}\sum_{n_z=0}^{\infty} \psi_{n_z}(z)\psi_{n_z}^*(z)\exp[-\beta\hbar\omega(n_z+0.5)], \tag{A1}$$

where the partition function, Q, of a linear harmonic oscillator is

$$Q = \sum_{n=0}^{\infty} \exp[-\beta\hbar\omega(n+0.5)] = [2\sinh(\beta\hbar\omega/2)]^{-1}, \tag{A2}$$

$\psi_{n_x}(x)$ is the wave function corresponding to energy level n_x for a 1D QHO corresponding to the x component, and $\omega = \sqrt{K/m}$.

Because the 3D QHO is spherically symmetric we expect the particle density to be conveniently expressed as $\rho(r)$, which is equivalent to

$$\rho(x) = \frac{1}{Q}\sum_{n_x=0}^{\infty} \psi_{n_x}(x)\psi_{n_x}^*(x)\exp[-\beta\hbar\omega(n_x+0.5)] \times \frac{1}{Q}\sum_{n_y=0}^{\infty} \psi_{n_y}(0)\psi_{n_y}^*(0)\exp[-\beta\hbar\omega(n_y+0.5)] \times \frac{1}{Q}\sum_{n_z=0}^{\infty} \psi_{n_z}(0)\psi_{n_z}^*(0)\exp[-\beta\hbar\omega(n_z+0.5)]. \tag{A3}$$

The wave functions of the 1D QHO are

$$\psi_n(x,t) = C_n H_n(\gamma x)\exp[-(\gamma x)^2/2]\exp(-iE_n t/\hbar), \tag{A4}$$

where the energy corresponding to each wave function is

$$E_n = \hbar\omega(n+0.5). \tag{A5}$$

In Eq. (A4) $i=\sqrt{-1}$, $\gamma=\sqrt{m\omega/\hbar}$, $C_n=\sqrt{\gamma/\pi^{1/2}2^n n!}$, and a recurrence relation is used for the Hermite polynomials:

$$H_0 = 1,$$

$$H_1 = 2\alpha x,$$

$$H_{n+1}(\alpha x) = 2\alpha x H_n(\alpha x) - 2nH_{n-1}(\alpha x). \tag{A6}$$

Note that although the particle density $(\psi_n(x)\psi_n^*(x))$ corresponding to individual linear harmonic oscillator states is not spherically symmetric, once the Boltzmann sum over states is performed the particle density is spherically symmetric, as required.

APPENDIX B: STATISTICAL MECHANICS OF PI RING POLYMERS

This appendix deals with the statistical mechanics of noninteracting PI ring-polymers in the canonical ensemble. We need only consider a single ring polymer. From Eq. (1) the partition function of one PI ring polymer is

$$Q_1 = \left(\frac{n\beta\lambda}{\pi}\right)^{3n/2} \int d\mathbf{R}\, \exp\{-\beta[H^{\mathrm{intra}}(\mathbf{R}) + H^{\mathrm{ext}}(\mathbf{R})]\}. \tag{B1}$$

From this we obtain the density profile of the entire ring polymer

$$\rho(\mathbf{R}) = \langle\delta(\mathbf{R}'-\mathbf{R})\rangle = \frac{1}{Q_1}\left(\frac{n\beta\lambda}{\pi}\right)^{3n/2} \int d\mathbf{R}' \times\exp\{-\beta[H^{\mathrm{intra}}(\mathbf{R}') + H^{ext}(\mathbf{R}')]\}\delta(\mathbf{R}'-\mathbf{R}) = Q_c^{-1}\exp\{-\beta[H^{\mathrm{intra}}(\mathbf{R}) + H^{ext}(\mathbf{R})]\}, \tag{B2}$$

where Q_c is the configurational part of the partition function Q_1. This proves that Eq. (5) is the correct expression for the canonical Helmholtz free energy functional because the minimum of Eq. (5) with respect to $\rho(\mathbf{R})$ gives Eq. (B2) when multiplied by $\exp(\beta\mu)$, where μ is a suitable Lagrange multiplier.

From Eq. (B1) we can also find the density profile of site i

$$\rho_i(\mathbf{r}) = \langle \delta(\mathbf{r}_i - \mathbf{r}) \rangle = \frac{1}{Q_1} \left(\frac{n\beta\lambda}{\pi} \right)^{3n/2} \int d\mathbf{R} \exp\{-\beta[H^{intra}(\mathbf{R}) + H^{ext}(\mathbf{R})]\} \delta(\mathbf{r}_i - \mathbf{r}), \tag{B3}$$

where $\mathbf{R} = (\mathbf{r}_1, \ldots, \mathbf{r}_n)$, which can be written

$$\rho_i(\mathbf{r}) = Q_c^{-1} e^{-\beta V(\mathbf{r})} \int d\mathbf{r}_{i-1} e^{-\beta V(\mathbf{r}_{i-1})} e^{-\beta n\lambda |\mathbf{r} - \mathbf{r}_{i-1}|^2} \int d\mathbf{r}_{i-2} e^{-\beta V(\mathbf{r}_{i-2})} e^{-\beta n\lambda r_{i-1.i-2}^2} \ldots \int d\mathbf{r}_1 e^{-\beta V(\mathbf{r}_1)} e^{-\beta n\lambda r_{21}^2}$$
$$\times \int d\mathbf{r}_{i+1} e^{-\beta V(\mathbf{r}_{i+1})} e^{-\beta n\lambda |\mathbf{r} - \mathbf{r}_{i+1}|^2} \int d\mathbf{r}_{i+2} e^{-\beta V(\mathbf{r}_{i+2})} e^{-\beta n\lambda r_{i+1.i+2}^2} \ldots \int d\mathbf{r}_n e^{-\beta V(\mathbf{r}_n)} e^{-\beta n\lambda r_{n-1.n}^2} \times e^{-\beta n\lambda r_{1.n}^2}. \tag{B4}$$

The open-ring approximation (ORA) deletes the last bond giving for the middle site

$$\rho_{(n+1)/2}(\mathbf{r}) = Q_c^{-1} e^{-\beta V(\mathbf{r})} [G_{(n-1)/2}(\mathbf{r})]^2, \tag{B5}$$

where G is given by Eq. (8).

Moreover, we can use a variant of the Percus trick appropriate for intamolecular distributions together with Eq. (B4) to obtain the bulk total intramolecular distribution function, $h_{i,n}^{\text{ring}}(r)$. So, by setting $e^{-\beta V(\mathbf{r}_1)} = \delta(\mathbf{r}_1)$ (which fixes site 1 at the origin) and $V(\mathbf{r}_{j\neq 1}) = 0$, which is appropriate for a uniform system, we first obtain the bulk intramolecular distribution function for site i,

$$h_{i,n}^{\text{ring}}(\mathbf{r}) = \rho_i(\mathbf{r}) \propto \int d\mathbf{r}_{i-1} e^{-\beta n\lambda |\mathbf{r} - \mathbf{r}_{i-1}|^2} \int d\mathbf{r}_{i-2} e^{-\beta n\lambda r_{i-1.i-2}^2} \ldots \int d\mathbf{r}_2 e^{-\beta n\lambda r_{32}} e^{-\beta n\lambda |\mathbf{r}_2|^2}$$
$$\times \int d\mathbf{r}_{i+1} e^{-\beta n\lambda |\mathbf{r} - \mathbf{r}_{i+1}|^2} \int d\mathbf{r}_{i+2} e^{-\beta n\lambda r_{i+1.i+2}^2} \ldots \int d\mathbf{r}_n e^{-\beta n\lambda r_{n-1.n}^2} e^{-\beta n\lambda |\mathbf{r}_n|^2}. \tag{B6}$$

Because of the convolution property of Gaussian functions, this can be written as

$$h_{i,n}^{\text{ring}}(r) = \left(\frac{\pi}{\beta\lambda} \right)^{3/2} h_{i-1}^{lin}(r) h_{n-i+1}^{lin}(r), \tag{B7}$$

where

$$h_j^{lin}(r) = \left(\frac{n\beta\lambda}{j\pi} \right)^{3/2} \exp(-n\beta\lambda r^2/j). \tag{B8}$$

For n odd the total function is then just

$$h_n^{\text{ring}}(r) = 2 \sum_{i=1}^{(n-1)/2} h_{i,n}^{\text{ring}}(r). \tag{B9}$$

This converges to the known [38] limiting result as $n \to \infty$

$$\frac{h_n^{\text{ring}}(r)}{n-1} \xrightarrow{n=\infty} \frac{2\beta\lambda}{\pi} \frac{\exp(-4\beta\lambda r^2)}{r}. \tag{B10}$$

For a chain polymer with n odd the total intramolecular distribution function relative to the middle site is simply

$$h_n^{\text{chain}}(r) = 2 \sum_{i=1}^{(n-1)/2} h_i^{\text{lin}}(r). \tag{B11}$$

[1] R. P. Feynman and A. R. Hibbs, *Quantum Mechanics and Path Integrals* (McGraw-Hill, New York, 1965).
[2] H. Lowen, J. Phys.: Condens. Matter **14**, 11897 (2002).
[3] D. Chandler and P. G. Wolynes, J. Chem. Phys. **74**, 4078 (1981).
[4] A. Broukhno, P. N. Vorontsov-Velyaminov, and H. Bohr, Phys. Rev. E **72**, 046703 (2005).
[5] C. E. Woodward, J. Chem. Phys. **94**, 3183 (1991).
[6] B. H. Zimm and W. H. Stockmayer, J. Chem. Phys. **17**, 1301 (1949).
[7] M. Bishop and C. J. Saltiel, J. Chem. Phys. **89**, 1159 (1988).
[8] H. Tanaka *et al.*, J. Am. Chem. Soc. **127**, 7511 (2005).
[9] P. Kowalczyk *et al.*, Langmuir **23**, 3666 (2007).
[10] A. Konstantakou *et al.*, Appl. Surf. Sci. **253**, 5715 (2007).
[11] C. Gu, G. H. Gao, and Y. X. Yu, J. Chem. Phys. **119**, 488 (2003).
[12] R. P. Sear and G. Jackson, Mol. Phys. **81**, 801 (1994).
[13] M. B. Sweatman, J. Phys.: Condens. Matter **15**, 3875 (2003).
[14] M. B. Sweatman (unpublished).
[15] S. Satyapal *et al.*, Catal. Today **120**, 246 (2007).
[16] M. Hirscher and B. Panella, Ann. Chim. (Paris) **30**, 519 (2005).
[17] S. K. Bhatia and A. L. Myers, Langmuir **22**, 1688 (2006).
[18] Q. Y. Wang and J. K. Johnson, Mol. Phys. **95**, 299 (1998).

[19] J. Turnbull and M. Boninsegni, Phys. Rev. B **76**, 104524 (2007).
[20] G. Stan and M. W. Cole, J. Low Temp. Phys. **110**, 539 (1998).
[21] P. Kowalczyk and J. M. D. MacElroy, J. Phys. Chem. B **110**, 14971 (2006).
[22] D. Chandler, J. D. McCoy, and S. J. Singer, J. Chem. Phys. **85**, 5971 (1986).
[23] D. Chandler, J. D. McCoy, and S. J. Singer, J. Chem. Phys. **85**, 5977 (1986).
[24] R. P. Feynman, *Statistical Mechanics* (McGraw-Hill, New York, 1972).
[25] G. A. Voth, Phys. Rev. A **44**, 5302 (1991).
[26] R. Evans, in *Fundamentals of Inhomogeneous Fluids*, edited by D. Henderson (Wiley, New York, 1992).
[27] Y. Rosenfeld, Phys. Rev. Lett. **63**, 980 (1989).
[28] E. Kierlik and M. L. Rosinberg, Phys. Rev. A **42**, 3382 (1990).
[29] S. Phan *et al.*, Phys. Rev. E **48**, 618 (1993).
[30] J. D. Weeks, D. Chandler, and H. C. Andersen, J. Chem. Phys. **54**, 5237 (1971); **54**, 5422 (1971).
[31] M. B. Sweatman, in *The Handbook of Theoretical and Computational Nanotechnology*, edited by M. Rieth and W. Schommers (American Scientific Publishers, Los Angeles, 2006), Vol. 5.
[32] M. B. Sweatman and N. Quirke, Mol. Simul. **31**, 667 (2005).
[33] M. B. Sweatman, Phys. Rev. E **63**, 031102 (2001).
[34] M. B. Sweatman, Phys. Rev. E **65**, 011102 (2002).
[35] J. Wang, J. K. Johnson, and J. Q. Broughton, J. Chem. Phys. **107**, 5108 (1997).
[36] H. Goldstein, *Classical Mechanics* (Addison-Wesley, Redwood City, CA, 1980).
[37] J. P. Hansen and I. McDonald, *Theory of Simple Liquids* (Academic Press, New York, 1990).
[38] J. D. McCoy, S. W. Rick, and A. D. J. Haymet, J. Chem. Phys. **92**, 3034 (1990).